Sub-arcsecond imaging with the International LOFAR Telescope

Astronomy & Astrophysics

Special issue

Subarcsecond view on the high-redshift blazar GB 1508+5714 by the International LOFAR Telescope[★]

A. Kappes[1] ⬤, P. R. Burd[1], M. Kadler[1], G. Ghisellini[2], E. Bonnassieux[1], M. Perucho[9,10], M. Brüggen[3], C. C. Cheung[4], B. Ciardi[5], E. Gallo[6], F. Haardt[2,7,8], L. K. Morabito[12,13], T. Sbarrato[2,11], A. Drabent[14], J. Harwood[15], N. Jackson[16], and J. Moldon[17]

[1] Institut für Theoretische Physik und Astrophysik, Universität Würzburg, Emil-Fischer-Straße 31, 97074 Würzburg, Germany
   e-mail: alexander.kappes@uni-wuerzburg.de
[2] INAF – Osservatorio Astronomico di Brera, Via Bianchi 46, 23807 Merate, Italy
[3] Hamburger Sternwarte, Universität Hamburg, Gojenbergsweg 112, 21029 Hamburg, Germany
[4] Space Science Division, Naval Research Laboratory, Washington, DC 20375, USA
[5] Max-Planck-Institut für Astrophysik, Karl-Schwarzschild-Straße 1, 85748 Garching b. München, Germany
[6] Department of Astronomy, University of Michigan, 1085 S University, Ann Arbor, MI 48109, USA
[7] INFN – Sezione Milano–Bicocca, Piazza della Scienza 3, 20126 Milano, Italy
[8] Dipartimento di Scienza e Alta Tecnologia, Università dell'Insubria, Via Valleggio 11, 22100 Como, Italy
[9] Departament d'Astronomia i Astrofísica, Universitat de València, C/ Dr. Moliner, 50, 46100 Burjassot, València, Spain
[10] Observatori Astronòmic, Universitat de València, C/ Catedràtic Beltrán 2, 46091 Paterna, València, Spain
[11] Dipartimento di Fisica G. Occhialini, Univ. Milano–Bicocca, P.za della Scienza 3, 20126 Milano, Italy
[12] Centre for Extragalactic Astronomy, Department of Physics, University of Durham, South Road, Durham DH1 3LE, UK
[13] Institute for Computational Cosmology, Department of Physics, University of Durham, South Road, Durham DH1 3LE, UK
[14] Thüringer Landessternwarte, Sternwarte 5, 07778 Tautenburg, Germany
[15] Centre for Astrophysics Research, University of Hertfordshire, College Lane, Hatfield AL10 9AB, UK
[16] Department of Physics and Astronomy, School of Natural Sciences, University of Manchester, Manchester M13 9PL, UK
[17] Instituto de Astrofísica de Andalucía (IAA, CSIC), Glorieta de las Astronomía, s/n, 18008 Granada, Spain

ABSTRACT

Context. Studies of the most distant active galactic nuclei (AGNs) allow us to test our current understanding of the physics present in radio-jetted AGNs across a range of environments, and probe their interactions with these environments. The decrease in apparent luminosity with distance is the primary difficulty to overcome in the study of these distant AGNs, which requires highly sensitive instruments.

Aims. Our goal is to employ new long wavelength radio data to better parametrise the broad-band spectral energy distribution (SED) of GB 1508+5714, a high-redshift ($z = 4.30$) AGN. Its high redshift, high intrinsic luminosity and classification as a blazar allow us to test emission models that consider the efficient cooling of jet electrons via inverse Compton losses in interactions with the dense cosmic microwave background (CMB) photon field at high redshifts. A significant detection of this effect in GB 1508+5714 may partly explain the apparent sparsity of high-redshift radio galaxies in wide-field surveys, detections of this kind are only becoming possible with the current generation of Square Kilometre Array (SKA) precursors.

Methods. We used the LOw-Frequency ARray (LOFAR) to image the long wavelength radio emission around the high-redshift blazar GB 1508+5714 on arcsecond scales at frequencies between 128 and 160 MHz. This allowed us to compare the spatially resolved structure with higher frequency observations, and construct spectral index maps to study the spectral properties of the different components.

Results. The LOFAR image shows a compact unresolved core and two resolved emission regions around 2 arcsec to the east and to the west of the radio core. We find structure consistent with previous Very Large Array (VLA) observations, as well as a previously unreported emission region to the east. The region in the west shows a spectral index of $-1.2^{+0.4}_{-0.2}$ while the region in the east indicates a spectral index of $\lesssim -1.1$. The radio core features a flat spectral index of 0.02 ± 0.01.

Conclusions. We interpret the arcsecond-scale radio structure of GB 1508+5714 as a FR II-like radio galaxy at a small viewing angle, and the western component as the region containing the approaching jet's terminal hot spot while the eastern diffuse component near the core can be interpreted as the counter-hot spot region. Our SED modelling shows that a scenario featuring significant quenching effects caused by interaction with the CMB provides a good description of the data, and notably explains the suppressed radio emission.

Key words. galaxies: active – galaxies: jets – galaxies: individual: GB 1508+5714 – radio continuum: galaxies – techniques: high angular resolution – techniques: interferometric

---

[★] The reduced images (FITS files) are only available at the CDS via anonymous ftp to cdsarc.u-strasbg.fr (130.79.128.5) or via http://cdsarc.u-strasbg.fr/viz-bin/cat/J/A+A/663/A44

1. Introduction

The remarkably bright nature of radio-jetted active galactic nuclei (AGNs) allows us to observe them at extreme redshifts and thus use their properties as an observational tracer of cosmological principles (Wang et al. 2021). Blazars, in particular, benefit from increased apparent luminosities due to relativistic boosting effects (Cohen et al. 2007b), and can thus be detected over a wide range of the electromagnetic spectrum, although at the cost of being observationally compact objects with small angles between their jets and the line of sight. Conversely, AGNs with radio jets that are at a larger angle to the line of sight are harder to detect with increasing distance. Because they can be observed over such a wide range of redshifts, they provide a unique insight into cosmology, galaxy evolution, and the evolution of AGNs (Dunlop & Peacock 1990; Georgakakis et al. 2017). In addition to probing the universe by observing targets at different redshifts, one should also account for differences in their evolutionary stage, the environment they are embedded in at that time, and their interactions with that environment. Many radio surveys have already been performed to investigate radio-loud AGN populations (e.g. Becker et al. 1995; Condon et al. 1998; Cohen et al. 2007a; Intema et al. 2017) and most find self-consistent relative number ratios of radio galaxies and blazars up to a redshift of ∼3 (Volonteri et al. 2011). Beyond this redshift, matters are complicated by uncertainties about the density evolution and the build-up of high black hole masses in the early universe (Blundell et al. 1999; Shankar et al. 2008). However, there seems to be a consensus that there is a relative lack of higher redshift radio galaxies even when accounting for evolutionary effects and detection limits (e.g. Wu et al. 2017; Hodges-Kluck et al. 2021, and references therein). The reason for the deficit is still not fully understood. The currently favoured explanation was suggested by Ghisellini et al. (2015): interaction of the extended radio emission with the cosmic microwave background (CMB) could efficiently quench the brightness of the extended radio lobes. Morabito & Harwood (2018) find evidence to support this model based on a comparison of simulations and observational data. In this scenario the CMB energy density dominates over the magnetic energy density at very high redshifts, so that the jet electrons interact with the CMB photons by inverse Compton (IC) scattering to cool, while the synchrotron radiation is suppressed. Although quenched, the steep-spectrum isotropic radiation of the extended structures could nevertheless be detected by telescopes operating in the long wavelength radio regime, which can test and guide the theoretical models. Ghisellini et al. (2015) proposed a number of suitable blazars to spotlight this issue, and published expected radio fluxes for different model parameters. The International LOFAR Telescope (ILT) (van Haarlem et al. 2013) offers the resolution, sensitivity, and observing wavelengths necessary to detect the extended emission from these blazars and to address the questions associated with its possible suppression. For this study, we processed and analysed one ILT observation of GB 1508+5714 at $z = 4.30$ (Hook et al. 1995), which is one of the most distant quasars with a detected X-ray jet (Yuan et al. 2003; Siemiginowska et al. 2003). Throughout the paper we use the following cosmological parameters: $H_0 = 71$ km s^{-1} Mpc^{-1}, $\Omega_m = 0.27$, and $\Omega_\Lambda = 0.73$, hence a luminosity distance of 39.8 Gpc and a conversion scale where $1''$ is about 6.9 kpc for the given source.

2. Observation and data reduction

We observed GB 1508+5714 on 15 June 2015 with the High Band Antenna (HBA) array of the international LOFAR telescope in dual outer mode[1], with the target positioned in the phase centre. Nine international stations[2] participated in this observation. The observation time was four hours covering 110 MHz to 190 MHz with applied time averaging of 16 s and a frequency channel width of 12.2 kHz. 3C196 was used as a flux density calibrator, with a ten-minute calibration observation prior to the target observation. After retrieving the data from the Long Term Archive (LTA), it was processed with PREFACTOR[3] (de Gasperin et al. 2019) version 3.0 to obtain calibration solutions for all stations using the calibrator, for polarisation alignment, clock, bandpass, and rotation measures. Phase solutions were found for the core and remote stations in the target field. This is a necessary step before continuing with the LOFAR- very long baseline interferometry (VLBI) pipeline[4], as described in Morabito et al. (2022), which uses these solutions to start the phase calibration of the international stations. After calibration, the final frequency coverage ranged between between 128 and 160 MHz in four sub-bands with 8 MHz bandwidth. This reduction in bandwidth was due to the presence of strong radio-frequency interference (RFI) in the data. The final full-band image has a central frequency of 144 MHz. The final time-averaging was 16 s. All core stations were combined to one virtual super station. The resultant reduction in data size allows for a simplified data handling and reduces I/O significantly (for more in-depth information regarding the whole LOFAR-VLBI pipeline, see Morabito et al. 2022). The remote stations RS503HBA, RS407HBA, and RS406HBA, and the international stations FR606HBA and SE607HBA were also removed from the dataset because of the poor data quality of visibilities associated with these stations. This could be due to problems at the station level at the time of observation or due to issues with the model of 3C196 used in the initial calibration. Diagnostic plots show good ionospheric conditions overall, which suggests that the issues were driven by the quality of the calibrator models at the time of reduction. If this is indeed the case, we expect the problem to disappear in the future when better models are available. The final (uv) coverage is shown in Fig. 1.

The imaging process was performed manually, with the addition of further self-calibration, using DIFMAP (Shepherd 1997). To test the robustness of our results, three parties performed the imaging process independently without prior knowledge of the expected structure; they also began the self-calibration with different starting models to ensure that the final result was independent of the initial model. The reality of structure in the eastern direction was verified by not including this structure in the model supplied to the self-calibration step, and was verified that it persisted despite this exclusion. Time and bandwidth smearing do not have a great impact on the final image because our target is located at the phase centre. We calculate the loss of intensity as a function of distance from the phase centre using the equations 18–43 for time smearing and 18–24 for bandwidth smearing from Bridle & Schwab (1999), with the final extinction curve shown in Fig. 2. We clearly see that smearing remains below 5% at a radial distance of about $6''$, which corresponds to the total extent of the source. This effect can thus be considered negligible in our subsequent analysis.

---

[1] Each core station has two HBA tile-fields, which are treated as individual stations in this mode.
[2] DE601HBA, DE602HBA, DE603HBA, DE604HBA, DE605HBA, DE609HBA, FR606HBA, SE607HBA, UK608HBA.
[3] Github repository https://github.com/lofar-astron/factor
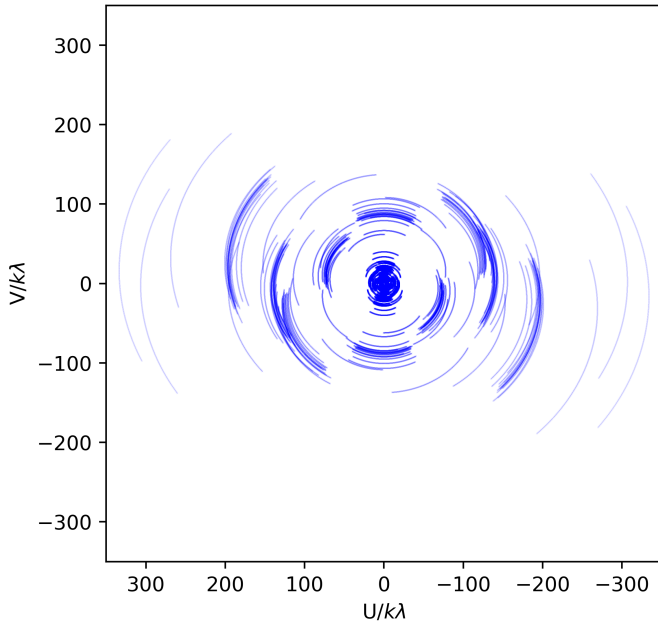[4] Github repository https://github.com/lmorabit/lofar-vlbi

Fig. 1. (*uv*) coverage for our International LOFAR Telescope data set at 144 MHz with the target GB 1508+5714 located in the phase centre observed on 15 June 2015 for 4 h.
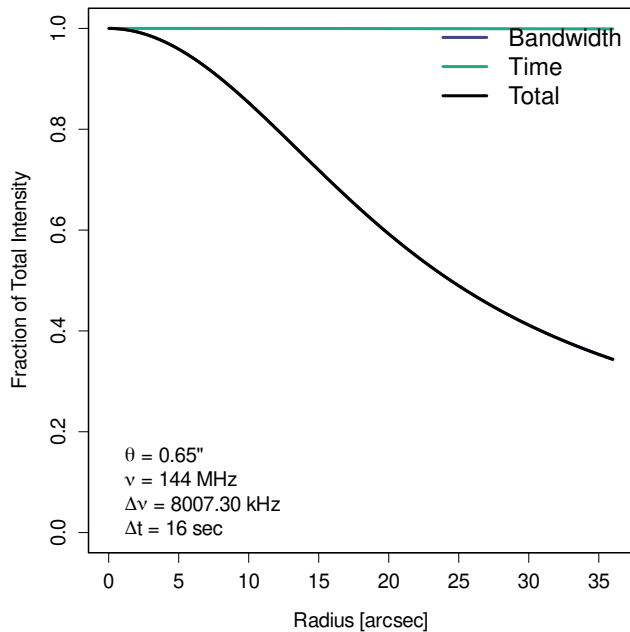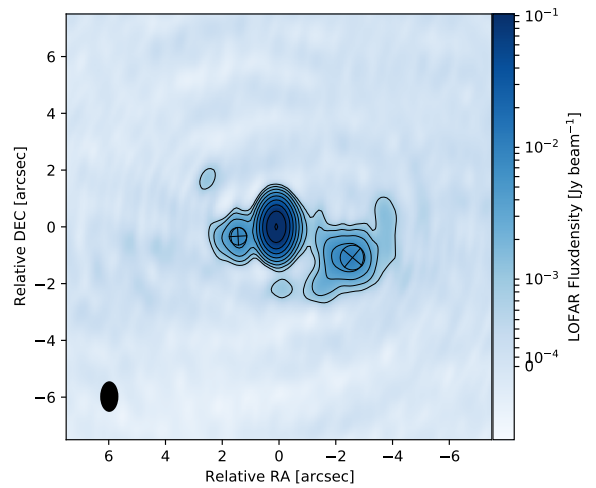

Fig. 3. LOFAR image of GB 1508+5714 at 144 MHz. The source brightness is colour- coded by flux-density, with the contour lines overlaid. The crossed circles indicate the modelled Gaussian components as hot spots. The contour levels are drawn at $(-1, 1, 2, 4, 8, ...)$ times 0.78 mJy beam^{-1}. The RMS is 0.13 mJy beam^{-1}. The restoring beam size (shown in the bottom left) is $1.08'' \times 0.643''$ with a position angle of $-0.27°$.

Fig. 2. Bandwidth and time smearing losses affecting the intensity for a point source in the pointing centre as a function of radius. Calculated after Bridle & Schwab (1999). The blue line indicating the bandwidth smearing is hidden by the black line indicating the total smearing.

3. Results

The final image is shown in Fig. 3. Most of the flux density (~86%) is contributed by the core component in the centre of the image. Significant bright and resolved emission is located east and west of the core, with the western component appearing brighter than the eastern one. The largest extent of the whole structure is about 6'' (~41 kpc). Previous observations with the *Karl G. Jansky* Very Large Array (VLA; Cheung 2004) are in

good agreement with our LOFAR image. For a direct comparison, Fig. 4 shows the contour lines from the VLA observation at 1.43 GHz overlaid on the LOFAR brightness distribution. The calibrated archival VLA data[5] came from a single five-minute snapshot observation in the A-configuration. This yielded a 10σ detection of the western component containing about 1.2 mJy. The core flux density amounts to (224 ± 11) mJy at 1.43 GHz at the time of the VLA observation. Despite the longer wavelength, the ILT image features a better angular resolution than the VLA. The eastern component shows a steep spectrum and is thus much fainter and appears unresolved at 1.43 GHz. The eastern component seen by LOFAR is not clearly detected by the VLA observation (see Cheung 2004). This component is not seen in the *Chandra* X-ray image either, even though the resolution is comparable to that of our ILT image (McKeough et al. 2016).

Reconvolving the LOFAR observation (beam size $1.08'' \times 0.643''$ at position angle, p.a., of $-0.27°$) with the beam parameters of the VLA observation (beam size $1.52'' \times 1.03''$ p.a. $-4.44°$ see contours in Fig. 5), we can see a very good visual agreement. The reconvolved LOFAR observation still shows a prominent resolved emission component to the east of the bright core. In comparison, the VLA observation only shows marginal evidence of an extension in this direction. This is consistent with the component featuring a steep spectral index.

Combining the reconvolved LOFAR data with the VLA data, performing an alignment correction and fitting a power law for each pixel with a flux value above a 2σ threshold (σ being 0.13 mJy beam^{-1} for the ILT image and 0.20 mJy beam^{-1} for the VLA image), we calculated the spectral index map shown in Fig. 5. Pixels for which the 2σ threshold is not met in either image are depicted in white. The core region shows a flat spectrum, which suggests that the variable flat-spectrum core was in a similar emission state during the LOFAR and VLA observations.

---

[5] https://hea-www.harvard.edu/XJET/img-data.cgi?1508_vla_2ghz_1995jul.txt
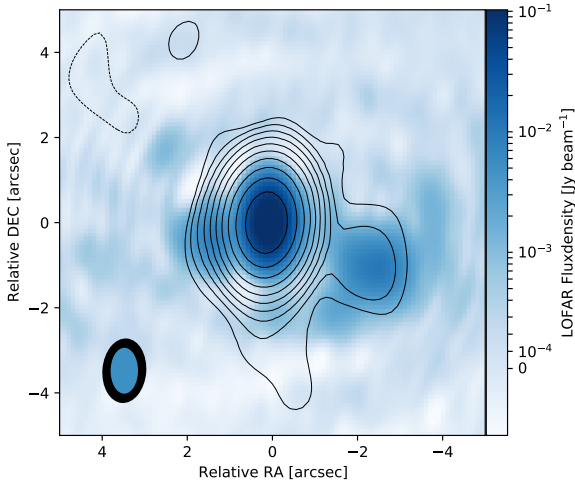
Fig. 4. Colour-coded LOFAR image of GB 1508+5714 at 144 MHz with the 1.43 GHz VLA contours from Cheung (2004) overlaid. The LOFAR and VLA restoring beams are shown in the bottom left corner as blue and black ellipses, respectively. The VLA contour levels are drawn at $(-1, 1, 2, 4, 8, \ldots)$ times 0.23 mJy beam^{-1}. The RMS in th VLA data is 0.20 mJy beam^{-1}. The restoring beam size is $1.52'' \times 1.03''$ with a position angle of $-4.44°$. The restored LOFAR beam size is $1.08'' \times 0.643''$ with a position angle of $-0.27°$.
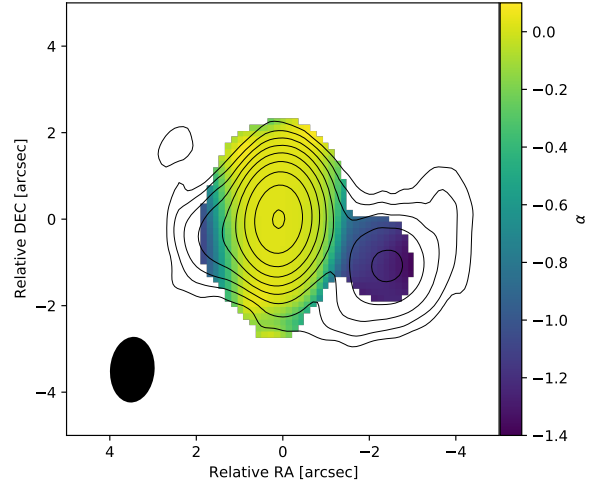

Fig. 5. Colour-coded spectral-index image between 144 MHz and 1.43 GHz. The contour levels show the flux-density distribution at 144 MHz with $(-1, 1, 2, 4, 8, \ldots)$ times 0.78 mJy beam^{-1}. The joint beam (shown bottom left corner) used to restore both the LOFAR and VLA images is $1.52'' \times 1.03''$ with a position angle of $-4.44°$.

We measure a steep spectral index[6] for the western component with a median value of -1.2 (min $= -1.4$, max $= -0.84$). Cheung et al. (2005) reported a spectral index of (-1.4 ± 0.2) between 1.4 and 5 GHz, which does not indicate any significant spectral break between 144 and 5 GHz. While the measured flux density of the eastern component in the VLA data is not significant enough to satisfy our flux threshold requirements, we can see a tendency of the same steepness, reaching $\alpha \lesssim -1.1$ at the easternmost edge of the spectral-index image. This value is an upper limit due to the non-detection by the VLA. Comparable values were reported previously for another high-redshift blazar in which subarcsec-scale emission features close to the core were identified as hot spots (Kappes et al. 2019). Considering that powerful quasars resemble rotated Fanaroff & Riley (1974) class II (hereafter FR-II) radio galaxies, in the unification model (Urry & Padovani 1995) observations of nearby FR-II radio galaxies at higher frequencies (accounting for K-correction) can be compared to our measurements. Here flatter spectral indices could be observed for hot spot regions (Ishwara-Chandra & Saikia 2000; Harwood et al. 2015).

Our LOFAR observation shows a total flux density of $F_{\nu,T} = (254 \pm 33)$ mJy. To determine the parameters of both components (eastern and western), we use a one-Gaussian model (major axis equals minor axis) component in each corresponding region to model the emission – see crossed circles in Fig. 3. We find $F_{\nu,W} = (20.5 \pm 2.6)$ mJy, for the western component with a diameter of about $0.87''$ ($\sim$6 kpc), and $F_{\nu,E} = (12.7 \pm 1.6)$ mJy, for the eastern component with a diameter of about $0.62''$ ($\sim$4 kpc). Similarly, we derive the flux density for the unresolved core component as $F_{\nu,\text{core}} = (218 \pm 28)$ mJy. The residual flux density of $F_{\nu,R} = (2.8 \pm 0.3)$ mJy remains unattributed in model components. The uncertainty on the residual flux density was calculated by considering the RMS in the residual image about $20''$ from the source, in a box with an area of about 200 beams.

---

[6] We define the spectral index α via $S_\nu \propto \nu^\alpha$, with S_ν radiative flux density.

This RMS was normalised by the square root of the number of pixels, and subsequently converted from mJy beam^{-1} to mJy. The total extended flux density is the sum of the three non-core emission contributions: $F_{\nu,\text{ext}} = (36.0 \pm 3.1)$ mJy.

4. Modelling

In this section we present the physical modelling done with our data as reference. This is necessary to determine the observational properties expected from a source with the same physical parameters but observed in the local Universe, where the CMB energy density is much smaller. These observational properties are plotted in our subsequent discussion, and indicated in Figs. 6, A.1–A.3 as 'no CMB'.

We focus on the flux density of the extended emission regions. In Ghisellini et al. (2015) these regions were assumed ad hoc to emit between 1 and 10% of the total jet power. We measure the value $\log_{10}(\nu F_{\nu,\text{ext}}) = -16.30^{+0.06}_{-0.05}$ in cgs units. If the spectral index α and the flux density of a certain region are known, then the corresponding specific luminosity can be determined as follows (Condon 1988):

$$L_{\text{region}} = \frac{F_{\text{region}} \cdot 4\pi \cdot (c \cdot z)^2}{H_0^2 \cdot (1+z)^{1-\alpha_{\text{region}}}}. \quad (1)$$

Assuming $\alpha = 0$ for the core, we derive $\log_{10}(L_{144\,\text{MHz,core}}) = 27.2$ (in cgs units). Spectral index values can vary across extended regions, so we use the minimum (-1.4) and maximum (-0.84) values as boundaries to calculate a range of intrinsic luminosities, accounting for the K-correction using the spectral index. The luminosity range for the extended emission is $\log_{10}(L_{144\,\text{MHz,ext}}) = 25.4$–$25.8$ (in cgs units), corresponding to 1.6–4.0% of the core luminosity. Following the canonical classification in Fanaroff & Riley (1974), the luminosity we calculate for GB 1508+5714 corresponds to the case of a FR-II radio galaxy (Owen & Ledlow 1994). The measurements of Owen & Ledlow (1994) are taken at 1.4 GHz for nearby sources (relative to GB 1508+5714) and so we must take the K-correction into account to compare results. Our observed frequency of about 144 MHz corresponds to an emitted frequency of about

Table 1. Adopted parameters for the jet model shown in Figs. 6–A.3.

Comp [1]	z [2]	M [3]	L_d [4]	R_{diss} [5]	R_{BLR} [6]	$P'_{e,jet,45}$ [7]	B [8]	Γ [9]	θ_V [10]	$P_{jet,45}$ [11]
jet	4.309	1.5e9	32	630	560	0.03	1.9	11	3	360

Notes. Column [1]: component; Col. [2]: redshift; Col. [3]: black hole mass in solar masses; Col. [4]: disc luminosity in units of 10^{45} erg s^{-1}; Col. [5]: distance of the dissipation region from the black hole in units of 10^{15} cm; Col. [6]: size of the broad line region, in units of 10^{15} cm; Col. [7]: power injected in the jet in relativistic electrons, calculated in the comoving frame, in units of 10^{45} erg s^{-1}; Col. [8]: magnetic field in G; Col. [9]: bulk Lorentz factor; Col. [10]: viewing angle in degrees; Col. [11]: total kinetic plus magnetic jet power, in units of 10^{45} erg s^{-1}. The values of the powers and the energetics refer to one jet. We assume, injected throughout the source $Q(\gamma)$ relativistic electrons with broken power law distribution, i.e. $Q(\gamma) \propto \gamma^{-1.5}$ below $\gamma = 200$ and $Q(\gamma) \propto \gamma^{-3}$ between $\gamma = 200$ and $\gamma = 4000$.
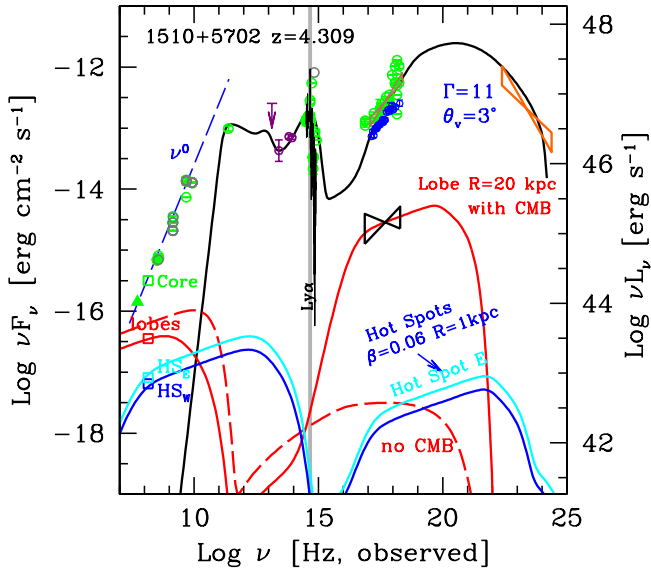

Fig. 6. SED of 1510+5702, from radio to γ-rays. The model shown (see parameters in Table 1) describes the non-thermal jet emission, the accretion disc and the molecular torus contributions (top black solid). All data are archival (https://tools.ssdc.asi.it/). For the hot spots and the lobes (as labelled; see corresponding model parameters in Table 2) this figure corresponds to model A. The lobe with a radius of 20 kpc is responsible for the diffuse X-ray emission observed by *Chandra* (black butterfly spectrum). The dashed red line is the lobe emission if there were no CMB. The vertical grey line gives the position of the Lyα line. The dashed blue line is not a fit of the radio spectrum of the core, but rather has been drawn to guide the eye. The labelled data points at 144 MHz are the LOFAR determinations from this work.

760 MHz, well below 1.4 GHz. Considering that the transition luminosity between FR-I and FR-II increases with decreasing frequency (Kembhavi & Narlikar 1999) we remain above the FR break: the FR-II association for GB 1508+5714 remains valid. GB 1508+5714 belongs to the class of flat spectrum radio quasars (FSRQs) which are considered the beamed counterparts of FR-II radio galaxies (Orr & Browne 1982) within the AGN unification scheme (Peacock 1987; Scheuer 1987; Barthel 1989; Urry & Padovani 1995). With recent findings (Mingo et al. 2019) on this canonical classification showing that FR-II radio galaxies can be up to three orders of magnitude below the traditional FR break, FR-I radio galaxies seem to be more strictly defined by lower luminosities; this would also suggest that GB 1508+5714 would more appropriately correspond to an FR-II object than an FR-I.

The broad-band spectral energy distribution (SED) of FSRQs is characterised by thermal emission (i.e. an accretion disc in the optical-UV, a torus in the IR and possibly a hot corona in the X-ray band) and non-thermal emission produced by a jet pointing at a small angle to the line of sight, and thus strongly boosted by relativistic beaming. FSRQs are typically strongly variable at different wavebands, and simultaneous variations are not uncommon (Meyer et al. 2019; Shukla & Mannheim 2020; MAGIC Collaboration 2020; Kramarenko et al. 2022; Acciari et al. 2021). The emission is therefore typically modelled as coming from a single region. In single-zone models, the emitting region must not be located too close to the accretion disc, to avoid being too compact and thus absorbing all the γ-ray emission in the γ–γ → e$^+$ e$^-$ process. Similarly, it cannot be too far from the accretion disc, to make it possible to explain the observed fast variability. This gives boundaries for the location of the source of emission at approximately $\sim 10^3$–10^4 Schwarzschild radii from the black hole (Liu & Bai 2006). All blazar SEDs exhibit two humps: one at low energy, due to synchrotron emission, and another at high energy, due to inverse Compton processes (although some hadronic processes may also contribute). In very powerful sources, such as GB 1508+5714, the first hump peaks in the sub-millimetre band, and the high-energy sources peak in the $\sim$MeV band. The last observable quantity is generally the accretion disc emission, peaking in the UV. In these sources we can thus model the disc emission to find estimates for its luminosity (and hence the accretion rate) and its black hole mass, independently of other methods such as emission line widths and luminosities. The uppermost data points in Fig. 6 show the SED produced by the accretion disc, the molecular torus and the emission from that part of the jet thought to produce most of the non-thermal radiation we see. Unfortunately, we do not have measurements in the appropriate IR band to constrain the molecular torus emission properties. The model, indicated as 'no CMB', shows the expected SED in the absence of the CMB. It can be seen that in this case the radio flux density would be enhanced and the X-ray emission severely depressed. This shows how a source with the same parameters would appear if it were nearby, where the CMB energy density is much lower (i.e. by a factor $(1 + z)^4 \sim 790$).

It should be noted that the core-dominated radio spectrum is flat (i.e. $F_\nu \propto \nu^0$, dashed blue line in Fig. 6) down to 50 MHz (de Gasperin et al. 2021). This emission is thought to be the superposition of the flux produced by larger and larger jet emitting zones, characterised by a self-absorption frequency ν_t inversely proportional to the emitting size (Blandford & Königl 1979). In the case of a conical jet, we should approximately have $\nu_t \propto 1/R_j$, where R_j is the distance from the black hole. Since the Doppler boost varies strongly with the viewing angle, we can conclude that the jet does not bend significantly, at least up to the regions producing the 50 MHz flux, otherwise the 50 MHz flux would not lie on the ν^0 line.

Table 2. Adopted parameters for the hot spot and lobe models shown in Figs. 6 and A.3.

Model [1]	Comp. [2]	R [3]	$\theta_{\rm v}$ [4]	β [5]	$P_{\rm e,45}$ [6]	B [7]	$\gamma_{\rm b}$ [8]	$\gamma_{\rm max}$ [9]	$\log E_{\rm e}$ [10]	$\log E_{\rm B}$ [11]	$E_{\rm e}/E_{\rm B}$ [12]
A	HS	1	3°, −177°	0.06	2.3	180	600	1e6	56.2	56.2	0.9
A	lobe	20	–	0	50	7	300	1e5	59.2	57.3	89
B	HS	2	3°, −177°	0.06	5.4	140	600	1e6	56.9	56.9	1
B	lobe	20	–	0	50	2.4	300	1.e5	59.2	56.4	630
C	HS	2.9	3°, −177°	0.06	600	7	400	1.e4	59.4	54.8	4e4
D	HS	2.9	3°, −177°	0.06	600	7	400	1.e4	59.4	54.8	4e4
D	lobe	20	–	0	1	12	400	1e4	57.8	57.7	1.2

Notes. Column [1]: Type of model; Col. [2]: component (HS = hot spot); Col. [3]: size in kpc; Col. [4]: viewing angle; Col. [5]: bulk velocity; Col. [6]: Power injected in relativistic electrons in units of 10^{45} erg s^{-1}; Col. [7]: magnetic field in µG; Cols. [8] and [9]: break and maximum Lorenz factor of the injected electron distribution; Col. [10]: logarithm of the total energy in relativistic electrons, in erg; Col. [11]: logarithm of the total energy in magnetic field, in erg; Col. [12]: total energy in relativistic electrons over total energy in magnetic field. The values of the powers and the energetics refer to *each* hot spot and lobe. The lobe flux shown in the figures corresponds to *two* lobes. We assume to inject throughout the source $Q(\gamma)$ relativistic electrons with a broken power law distribution, i.e. $Q(\gamma) \propto \gamma$ below $\gamma = \gamma_{\rm b}$ and $Q(\gamma) \propto \gamma^{-2.7}$ between $\gamma_{\rm b}$ and $\gamma_{\rm max}$.

This implies $R_{\rm j}(50\,{\rm MHz}) \sim 1.3$ kpc if we assume that the flux at 300 GHz is produced in the jet region emitting the rest of the jet spectrum. All the jet parameters, which are listed in Table 1 for convenience, are very similar to the blazars detected by the Large Area Telescope (LAT) on board the *Fermi* satellite (Atwood et al. 2009) and analysed in Ghisellini & Tavecchio (2015). The jet power ($P_{\rm jet} \sim 3 \times 10^{47}$ erg s^{-1}) is dominated by the bulk motion of cold protons (assumed to be equal in number to the emitting electrons, i.e. assuming no significant contribution from electron–positron pairs). The lower limit to $P_{\rm jet}$ is 10^{46} serg s^{-1}, which is the total power in radiation emitted by the jet.

We note that the 'jet–hot spots–lobe' models are a simplified representation of a likely complex reality. In particular, the lobe and the hot spots are idealised to be spheres homogeneously filled with tangled magnetic fields and relativistic particles, without internal gradients. When dealing with extended sources at high redshifts, the contribution of the CMB becomes important since it can be the dominant source of seed photons to be scattered at high energies. Relativistic electrons can inverse Compton scatter their own synchrotron photons, called synchrotron self-Compton (SSC), and also the CMB photons. In the latter case we call this the external Compton process. The energy density of the CMB increases with redshift as $(1 + z)^4$, and we have equipartition between the magnetic ($U_{\rm B}$) and the CMB ($U_{\rm CMB}$) energy densities for a magnetic field value $B_{\rm eq}$ given by

$$B_{\rm eq} = 3.26 \times 10^{-6}(1 + z)^2{\rm G} = 9.2 \times 10^{-5}\left[\frac{(1 + z)}{1 + 4.309}\right]^2 {\rm G}. \quad (2)$$

For magnetic fields smaller than $B_{\rm eq}$, we have $U_{\rm CMB} > U_B$, and the high-energy (typically X-ray) luminosity produced by the external Compton is greater than the synchrotron luminosity.

A diffuse extended component has been measured in X-rays by *Chandra* (Siemiginowska et al. 2003; Yuan et al. 2003, butterfly spectrum in Fig. 6). Assuming that this X-ray component is produced by the external Compton process, the ratio of this X-ray luminosity to the extended radio luminosity is a measure of the ratio $U_{\rm CMB}/U_{\rm B}$. As illustrated in Fig. A.1, the ratio is between two and three orders of magnitude. We therefore can find an upper limit for the value of the magnetic field of the extended

(hot spots and/or lobes) components $B_{\rm ext}$

$$\frac{L_{\rm X,ext}}{L_{\rm syn}} \sim \frac{U_{\rm CMB}}{U_{\rm B}} \rightarrow B_{\rm ext} \lesssim \left[\frac{8\pi U_{\rm CMB}}{L_{\rm X,ext}/L_{\rm syn}}\right]^{1/2}, \quad (3)$$

giving $B_{\rm ext} \lesssim 3$ µG for $L_{\rm X,ext}/L_{\rm syn} = 10^3$. This estimate is independent of the volume of the region emitting the diffuse X-rays. Therefore, it can be applied to both the lobe and the hot spots, depending on which structure is responsible for the diffuse X-ray flux.

The power in relativistic electrons, $P_{\rm e}$ injected into the hot spots and the lobes can be derived by requiring that they produce the observed X-ray luminosity $L_{\rm X,ext}$. As long as the radiative cooling is dominated by the CMB, $P_{\rm e}$ is also independent from the volume of the lobe. Some subtleties arise from the fact that we do not assign a given and fixed particle distribution, but rather find it self-consistently through a continuity equation that accounts for the cooling terms (synchrotron, SSC, external Compton, adiabatic). Therefore, we specify a priori the total power injected in the relativistic electron population and its shape (a broken power law, very hard at low energies and steeper after a break), and hence find the emitting distribution. This procedure is crucial if we want to establish the effects of the CMB. When the CMB dominates the radiative cooling, it steepens the particle distribution above the energy cooling break $E_{\rm cool}$, corresponding to the synchrotron frequency $\nu_{\rm cool}$. Above this frequency the synchrotron emission is depressed. We refer the reader to Ghisellini et al. (2014, 2015) for a complete description and the relevant equations of the model.

5. Discussion

In this section, we compare our observations to the predictions reported in the literature (Ghisellini & Tavecchio 2009; Ghisellini et al. 2014, 2015) regarding the proposed CMB quenching mechanism that was suggested to explain the apparent sparseness of high-redshift ($z \gtrsim 4$) misaligned jetted AGNs in radio surveys. For completeness, a further three models are presented in the Appendix; these were excluded in the process of our analysis in favour of the one presented here. All these physical scenarios for GB 1508+5714 involve a FR-II-like source structure (pointed at a small angle to the line of sight) with varying lobe and hot spot contributions to the observed radio and

X-ray data. While it is straightforward to identify the core of the source, the two components observed east and west of the core are considered extended lobes. The brightest points in these lobes likely contain the hot spots, but their physical sizes might well be smaller than the beam size in our observation[7], and it is unclear what fraction of the emission should be attributed to lobe emission versus hot spots. There are cases where they might be interpreted as two individual hot spots, such as Kappes et al. (2019), but the situation was clearer in that case than for GB 1508+5714. The additional residual radio flux density measured by LOFAR (amounting to $F_{\nu,R}$ =2.8 mJy) is estimated by taking the difference between the total flux density and the flux densities of the resolved components. This can be attributed to artefacts introduced during calibration, or non-Gaussian extensions of the lobes or hot spots. Artefacts are commonplace in radio-interferometric images, and so we proceed with the postulate that these extensions are not real features. For the sake of completeness, the possibility that they are is explored in other possible models (denoted B,C, and D) in Appendix A. We therefore refer to the model in which the non-Gaussian extensions are dismissed as not real features as model A.

Model A. We consider that the two lobes dominate the western and eastern components and contain a faint unresolved hot spot each. We limit the maximum possible brightness of the two hot spots to $\lesssim$4.3 mJy and $\lesssim$5.3 mJy, respectively, in order to not exceed the local surface brightness of their two lobes. The total flux density for both lobes accounts for 23.6 mJy. In this model the two strong lobes dominate the X-ray emission (although the *Chandra* image suggests a more efficient X-ray production associated with the western lobe). Figure 6 shows the SED for this model. In this case the two strong lobes are dominating both the total extended radio flux east and west of the core and the diffuse X-ray flux. As listed in Table 2, the lobes are not very far from equipartition ($E_e/E_B \sim 89$) and the power required to energise this structure is 5×10^{46} erg s^{-1}. The energetics of the hot spots are consistent with a state of equipartition.

Although we favour model A, which is a self-consistent and physically motivated representation of the observed properties of GB 1508+5714, it does not result in the tightest constraints on hot spot luminosities nor does it allow us to derive constraints on hot spot advance speeds, which depends on differences in Doppler boosting. This was a motivation to considering the models B, C, and D shown in the Appendices; the relevant calculations that derive from the best-fit values for these models are given in Appendices B and C. Properly constraining these models, however, will require creating higher-quality interferometric images than was possible with the quality of the data available to us; they are therefore only given as a point of reference, and we do not consider them to have scientific value at this time. In all cases, we can state that CMB quenching must be present as expected to explain the observations.

6. Conclusion

New high-resolution images taken by the ILT allow a novel view on the high-redshift blazar GB 1508+5714 showing a previously unseen component in the eastern direction. By reconvolving the

ILT data with the VLA beam, we were able to create a spectral index map, from which we derive constraints on the spectral indices of individual components: $-1.2^{+0.4}_{-0.2}$ for the western component; steeper than -1.1 for the eastern region; 0.023 ± 0.007 for the core. We then considered a model where the hot spots are unresolved in the detected components and are blended by the lobe emission. The X-ray emission originates from the lobes and is partially (eastern lobe) blended by the bright core region. For completeness we considered three other possible interpretations that are worked out in Appendix A. The preferred model's results are consistent with hot spots in a state of equipartition and lobes nearly so. In all models we can confirm the necessity of CMB quenching processes as proposed by Ghisellini et al. (2015). We note the need for more observations of these sources, especially with the current more mature ILT configuration which features more international stations, resulting in a more sensitive instrument but more importantly in a much more stable instrument overall. This will allow future observations to result in much higher-quality data than was possible for the ILT to create in 2015, when our observation was taken: in turn, it could make a full investigation and characterisation of the models discussed in the appendix possible as they were dismissed primarily due to problems with data quality. Nevertheless, in this paper we have shown that it is possible to study high-z blazars with the 2015 configuration of the ILT; any observations performed after the time of publication can only provide superior observational constraints. In the future, expanding the sample of high-z blazars resolved in multi-frequency will allow us to conduct a statistical study of the population.

References

Acciari, V. A., Ansoldi, S., Antonelli, L. A., et al. 2021, MNRAS, 504, 1427
Atwood, W. B., Abdo, A. A., Ackermann, M., et al. 2009, ApJ, 697, 1071
Barthel, P. D. 1989, ApJ, 336, 606
Becker, R. H., White, R. L., & Helfand, D. J. 1995, ApJ, 450, 559
Begelman, M. C., & Cioffi, D. F. 1989, ApJ, 345, L21
Blandford, R. D., & Königl, A. 1979, ApJ, 232, 34
Blundell, K. M., Rawlings, S., & Willott, C. J. 1999, AJ, 117, 677
Bridle, A. H., & Schwab, F. R. 1999, ASP Conf. Ser., 180, 371
Cheung, C. C. 2004, ApJ, 600, L23
Cheung, C., Wardle, J., & Lee, N. 2005, 22nd Texas Symp. on Relativistic Astrophysics, eds. P. Chen, E. Bloom, G. Madejski, et al. (Palo Alto, CA: SLAC), 480
Cohen, A. S., Lane, W. M., Cotton, W. D., et al. 2007a, AJ, 134, 1245
Cohen, M. H., Lister, M. L., Homan, D. C., et al. 2007b, ApJ, 658, 232
Condon, J. J. 1988, Radio Sources and Cosmology (New York, NY: Springer New York), 641
Condon, J. J., Cotton, W. D., Greisen, E. W., et al. 1998, AJ, 115, 1693
Croston, J. H., Hardcastle, M. J., Harris, D. E., et al. 2005, ApJ, 626, 733
de Gasperin, F., Dijkema, T. J., Drabent, A., et al. 2019, A&A, 622, A5
de Gasperin, F., Williams, W. L., Best, P., et al. 2021, A&A, 648, A104
Dunlop, J. S., & Peacock, J. A. 1990, MNRAS, 247, 19
Fanaroff, B., & Riley, J. 1974, MNRAS, 167, 31P
Georgakakis, A., Aird, J., Schulze, A., et al. 2017, MNRAS, 471, 1976

---

[7] For a simple conical jet model, we would expect a hot spot diameter of about 2.5 arcsec, assuming a jet inclination angle of 3° and an opening angle of 2.5°. For larger inclinations and/or smaller intrinsic opening angles (e.g. Pushkarev et al. 2009) this can yield substantially smaller angular scales.

Ghisellini, G., & Tavecchio, F. 2009, MNRAS, 397, 985
Ghisellini, G., & Tavecchio, F. 2015, MNRAS, 448, 1060
Ghisellini, G., Celotti, A., Tavecchio, F., Haardt, F., & Sbarrato, T. 2014, MNRAS, 438, 2694
Ghisellini, G., Haardt, F., Ciardi, B., et al. 2015, MNRAS, 452, 3457
Hardcastle, M. 2015, Kiloparsec-Scale AGN Jets (Berlin: Springer), 414, 83
Harwood, J. J., Hardcastle, M. J., & Croston, J. H. 2015, MNRAS, 454, 3403
Hodges-Kluck, E., Gallo, E., Ghisellini, G., et al. 2021, MNRAS, 505, 1543
Hook, I. M., McMahon, R. G., Patnaik, A. R., et al. 1995, MNRAS, 273, L63
Intema, H. T., Jagannathan, P., Mooley, K. P., & Frail, D. A. 2017, A&A, 598, A78
Ishwara-Chandra, C. H., & Saikia, D. J. 2000, MNRAS, 317, 658
Jeyakumar, S., & Saikia, D. 2000, MNRAS, 311, 397
Kappes, A., Perucho, M., Kadler, M., et al. 2019, A&A, 631, A49
Kembhavi, A. K., & Narlikar, J. V. 1999, Radio Properties (Cambridge: Cambridge University Press), 214
Kramarenko, I. G., Pushkarev, A. B., Kovalev, Y. Y., et al. 2022, MNRAS 510, 469
Liu, H. T., & Bai, J. M. 2006, ApJ, 653, 1089
MAGIC Collaboration (Acciari, V. A., et al.) 2020, A&A, 637, A86
McKeough, K., Siemiginowska, A., Cheung, C. C., et al. 2016, ApJ, 833, 123
Meyer, M., Scargle, J. D., & Blandford, R. D. 2019, ApJ, 877, 39
Mingo, B., Croston, J. H., Hardcastle, M. J., et al. 2019, MNRAS, 488, 2701
Morabito, L. K., & Harwood, J. J. 2018, MNRAS, 480, 2726
Morabito, L. K., Jackson, N. J., Mooney, S., et al. 2022, A&A, 658, A1
Orr, M. J. L., & Browne, I. W. A. 1982, MNRAS, 200, 1067
Owen, F. N., & Ledlow, M. J. 1994, ASP Conf. Ser., 54, 319
Peacock, J. 1987, in Astrophysical Jets and Their Engines (Berlin: Springer), 185
Perucho, M., Martí, J.-M., Quilis, V., & Borja-Lloret, M. 2017, MNRAS, 471, L120
Perucho, M., Martí, J.-M., & Quilis, V. 2019, MNRAS, 482, 3718
Pushkarev, A., Kovalev, Y., Lister, M., & Savolainen, T. 2009, A&A, 507, L33
Scheuer, P. A. G. 1974, MNRAS, 166, 513
Scheuer, P. A. G. 1987, in Superluminal Radio Sources, eds. J. A. Zensus, & T. J. Pearson (Cambridge: Cambridge University Press), 104
Scheuer, P. 1995, MNRAS, 277, 331
Shankar, F., Weinberg, D. H., & Miralda-Escudé, J. 2008, ApJ, 690, 20
Shepherd, M. C. 1997, ASP Conf. Ser., 125, 77
Shukla, A., & Mannheim, K. 2020, Nat. Commun., 11, 4176
Siemiginowska, A., Smith, R. K., Aldcroft, T. L., et al. 2003, ApJ, 598, L15
Urry, C. M., & Padovani, P. 1995, PASP, 107, 803
van Haarlem, M. P., Wise, M. W., Gunst, A. W., et al. 2013, A&A, 556, A2
Volonteri, M., Haardt, F., Ghisellini, G., & Ceca, R. D. 2011, MNRAS, 416, 216
Wang, F., Yang, J., Fan, X., et al. 2021, ApJ, 907, L1
Wu, J., Ghisellini, G., Hodges-Kluck, E., et al. 2017, MNRAS, 468, 109
Yuan, W., Fabian, A. C., Celotti, A., & Jonker, P. G. 2003, MNRAS, 346, L7

Appendix A: Discussion for models B, C, and D

Following the discussion in section 5 we present the three models that we were able to discard in the process of our scientific analysis of the data, but nevertheless find valuable to discuss for the sake of completeness. These models do not make clear a priori assumptions on whether the hot spots or the lobes dominate the observed X-ray emission. With the parameters derived from the individual morphological interpretations and the modelling of the accretion disc, jet, hot spots and lobes we present the results for the individual models B, C, and D.

Model B — Here we assume that the residual 2.8 mJy radio flux density is produced by two lobes each with a radius of 20 kpc (40 kpc corresponds to the largest extent of the source in Fig. 3). We further assume that these lobes produce the diffuse Chandra X-ray emission. We interpret the resolved components in the east and west as hot spots. Due to the assumption we have made, it follows that this model excludes the possibility that the hot spots contribute to the diffuse X-ray flux in any capacity. The corresponding SED and model are shown in Fig. A.1. As discussed above (Eq. 3), the magnetic field strength must be less than the order of ~microGauss, regardless of the size of the lobes. This very small value, together with the requirement to produce a large diffuse X-ray luminosity, results in best-fit models that can only be far from equipartition. In our case $E_e/E_B \sim 630$. The impact of the CMB can be seen by examining the SED of the lobe in the absence of the CMB. The first effect is a huge reduction of the X-ray flux, due to the absence of seed CMB photons. The radio spectrum is also drastically different because the particle distribution would have a radiative cooling break at much higher energies. Therefore, the emission slope in the radio band would continue to be flat up to the sub-millimetre band.

The two hot spots have similar, but not identical, fluxes. Model B allows us to explain this by invoking the different Doppler boosts due to the bulk velocity of the hot spots, assumed equal in all respects but the viewing angle. We thus model them both as having a physical radius of 2 kpc. If the hot spots do not contribute significantly to the diffuse X-ray flux, we cannot find a unique solution. This strengthens the hypothesis made in Model A that there should be equipartition between the relativistic electron and the magnetic field total energy in the hot spot. This constraint, listed in Table 2, is also a strong enough constraint to fix the value of the power injected in each lobe, which amounts to ~1/65 of the total jet power (emitted synchrotron radiation in our respective radio band). For consistency with the viewing angle of the jet, we assume $\theta = 3°$ and $\theta = 180° - 3°$ for the western and eastern hot spot, respectively (Ghisellini et al. 2015).

Model C — Here we assume that the lobes do not contribute at all to the observed radio emission (i.e. that they emit only below the ILT sensitivity threshold). The diffuse X-ray flux is then produced entirely by the eastern and western components identified as hot spots, and the residual emission in the image is entirely unphysical. We note that the Chandra image (Siemiginowska et al. 2003; Yuan et al. 2003) shows a resolved component corresponding to the western hot spot, but no corresponding counterpart in the east. This discrepancy could be explained if the eastern hot spot's X-ray emission were blended with the dominant core emission. The SED for this model is shown in Fig. A.2. The hot spots' magnetic field value

is then 7μG, which implies that the magnetic field is very far from equipartition: $E_e/E_B \sim 4 \times 10^4$. The power that the jet must supply to the hot spot in the form of relativistic electrons is very large, amounting to $P_e \sim 6 \times 10^{47}$ erg s^{-1}, even larger than P_{jet}. This is due to the fact that even the highest energy electrons cannot radiatively cool on a timescale shorter that the adiabatic timescale $\sim R/c$. The emission process is therefore very inefficient, requiring a large number of relativistic electrons (and thus a large injected power), leading to a case very far from equipartition.

Model D — Here we consider that the lobes are responsible for the 2.8 mJy residual flux density, but that the bulk of the extended radio emission is to be attributed to two strong hot spots. In contrast to model B, the lobes do not contribute significantly to the diffuse X-ray emission, which is assumed to be dominated by the hot spots. Figure A.3 shows the SED for this model. This allows it to be close to equipartition; however, the problems associated with the hot spot properties of model B remain.

In conclusion, model A is the only one that simultaneously satisfies the equipartition condition for the hot spots and the lobes near them. It is also by far the least energetically demanding model. Model B only reaches equipartition within the hot spots, but not the lobes; models C and D do not reach equipartition anywhere. This is the basis on which all three of the models described in this section are dismissed in favour of model A.

Appendix B: Hot spot advance speeds

Although models B, C, and D must be dismissed because of their failure to satisfy equipartition conditions, they have the very attractive ability (if applicable) to use their distinction between hot spot and lobe emission to estimate the advance speed of the hot spot components. In this section, we describe what the current results of such an analysis would be, in order to demonstrate what could become possible if future observations are able to provide data of sufficient quality to constrain these models without relying on equipartition conditions. Parameters such as the hot spot speed and the jet inclination angle can be constrained using the ratio of the hot spot flux densities if we use the simplified model of a symmetric two-sided jet:

$$R = \frac{F_{\nu,W}}{F_{\nu,E}} = \left(\frac{1 + \beta \cos(\theta)}{1 - \beta \cos(\theta)} \right)^{3-\alpha} \quad . \tag{B.1}$$

Here $v = \beta c$ is the speed of two symmetric blobs, where θ is the viewing angle of the approaching blob. From the flux density of the hot spot components within models B, C, and D, we obtain $R = 1.65^{+0.03}_{-0.05}$. For illustrative purposes, we initially consider a broad inclination angle between $0° \leq \theta \leq 25°$ and consider three representative cases for hot spot speeds, $\beta_{HS} = 0.053, 0.060$ and 0.067, which are colour-coded in Fig. B.1. The spectral index in the range obtained from Fig. 5 is encoded in the opaqueness of each colour, where a more saturated tone indicates a steeper α ($\alpha_{min} = -1.4$; $\alpha_{max} = -0.84$). A lower limit of $\theta_{min} \gtrsim 2°$ is obtained by comparing the measured projected size of the source with the largest known radio galaxies (~ 1 Mpc; Jeyakumar & Saikia 2000) by assuming that these represent an upper limit on the physical size a radio galaxy can have. The SED of the core (see Sect. 4) then suggests that the inclination angle of the inner
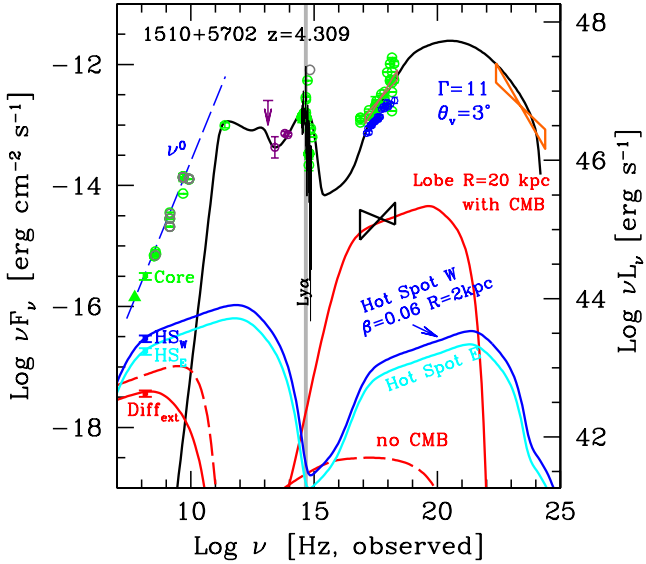
Fig. A.1. As Fig. 6, but for model B. The hot spots are 2 kpc in size with a weaker magnetic field. All parameters are given in Table 2, together with those adopted for the lobes.

Fig. A.2. As Fig. 6, but for model C. The diffuse X-ray emission observed by Chandra is produced by the hot spots, and there are no lobes. We also show how the flux of the western hot spot would appear if there were no CMB. This shows that most of the X-ray diffuse flux is the result of external Compton process with the CMB photons, while the SSC component is very weak. At high energies the flux is dominated by the second-order Compton scatterings (second IC). The parameters adopted for the hot spots are given in Table 2.

jet to be around $\theta_{\text{SED}} \approx 3°$. While the inclination angle can be deviated further along the jet due to various effects (e.g., jet bending or precession), we see that the estimates of hot spot speeds within this model depend only weakly on the orientation angle and thus cannot deviate much from about $0.06\,c$.

Appendix C: Jet age

The evolutionary stage, and therefore the age, of a jet is an important characteristic. It can be estimated from its size, assuming that estimates of the hot spot advance speed derived from SED modelling are accurate and that this advance speed is constant in time. Despite the failures of models B, C, and D, we note that their estimates of the hot spot advance speed should be correct to within an order of magnitude (Scheuer 1995). The results of the following derivation depend linearly on speed; they too are expected to be correct to within an order of magnitude. Perucho et al. (2019) shows that numerical simulations of jet evolution in hot galactic atmospheres find that jets may accelerate down the pressure gradient of the galactic halo, and that they also undergo deceleration as the dentist drill effect develops (Scheuer 1974). The assumption of a constant velocity is thus known not to hold, but it can still provide a good first-order estimate. In this case, the age of the jet is given by
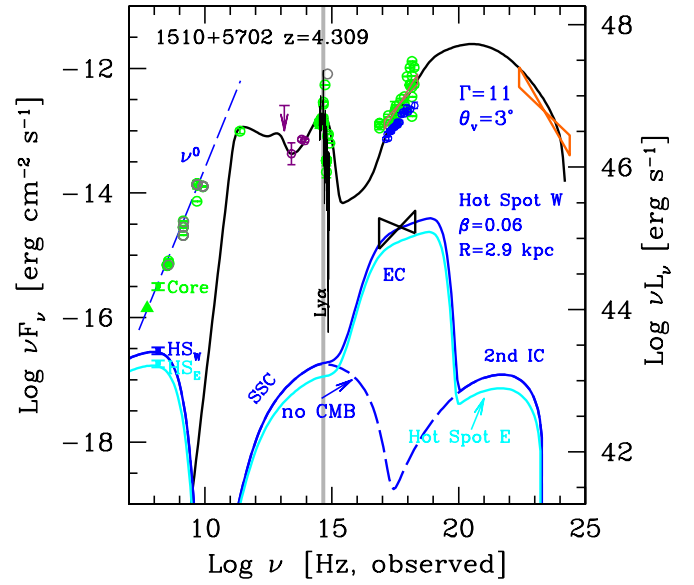
$$t_{\text{jet}} \simeq 7.3 \times 10^6 \left(\frac{L_{\text{jet}}}{135\,\text{kpc}}\right)\left(\frac{0.06}{\beta_{\text{HS}}}\right)\,\text{yr}, \tag{C.1}$$

where L_{jet} is the jet length.

Since powerful relativistic jets inject a large part of their energy into lobe pressure (see Perucho et al. 2017), we can use the following expression, derived from dimensional arguments (see Begelman & Cioffi 1989; Perucho et al. 2017), to estimate the lobe pressure from the power and age of the jet as well as the volume of the lobe,

$$p_{\text{lobe}} = \kappa \frac{P_{\text{jet}}\, t_{\text{jet}}}{V_{\text{lobe}}}, \tag{C.2}$$

with $\kappa \simeq 0.4$ for relativistic jets (see Perucho et al. 2017). Approximating the lobe volume to that of a cylinder of length L and an estimated lobe radius of 20 kpc, taking $P_{\text{jet}} \simeq 10^{47}$ erg/s, and using the previous expression for the age of the jet, we obtain

$$p_{\text{lobe}} \simeq 1.8 \times 10^{-9} \left(\frac{\kappa}{0.4}\right)\left(\frac{P_{\text{jet}}}{10^{47}\,\text{erg/s}}\right)\left(\frac{\beta_{\text{HS}}}{0.06}\right)^{-1}\left(\frac{R_{\text{lobe}}}{20\,\text{kpc}}\right)^{-2}\,\text{erg/cm}^3. \tag{C.3}$$

The expression is independent of jet length because the contributions of both jet age and lobe volume cancel out. This estimate of lobe pressure is two orders of magnitude higher than that of the magnetic pressure implied by the modelled magnetic field strengths ($\simeq 2 \times 10^{-12}$ erg/cm³). This could be explained by considering that the lobe pressure derived here would also include the contribution of the thermal population, which can
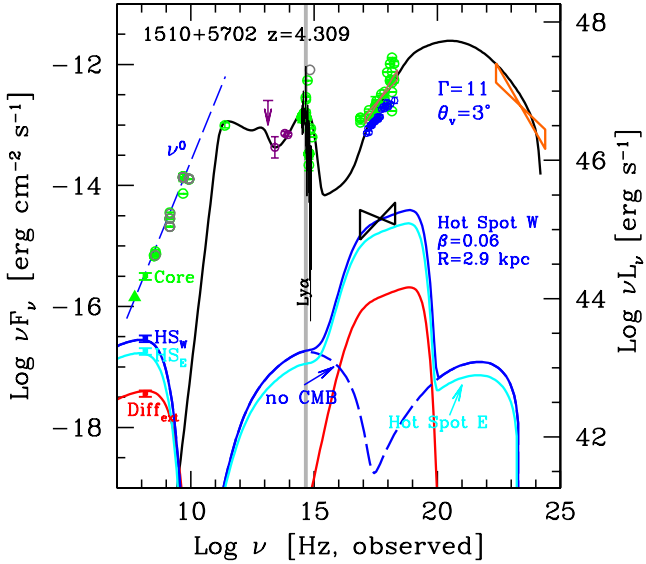
Fig. B.1. Ratio of the flux of western to eastern components, R, as a function of the inclination angle, θ, and the hot spot speed, β_{HS}. The different hot spot speeds are colour-coded; the spectral index is given by the opaqueness of the different regions (a more saturated tone is a steeper $-0.84 > \alpha > -1.4$). The dashed horizontal lines constrain the parameter space with R within its error (see Eq. B.1).The θ_{min} value is determined by comparing the measured projected size with large radio galaxies. The θ_{SED} value shows the suggested inclination angle of the inner jet by the SED.

Fig. A.3. As Fig. 6, but for model D. The diffuse X-ray emission observed by Chandra is produced by the hot spots, but we assume that the lobes exist, and emit 2.8 mJy flux density at 144 MHz. We then study the parameters that a 20 kpc lobe must have in order to produce the radio, but not the observed X-rays. The hot spots have the same parameters as in Fig. A.2 and are given in Table 2, together with those adopted for the lobes.

dominate over both the electron and magnetic pressures (Croston et al. 2005). Hardcastle (2015) provides evidence that the magnetic field should be around equipartition with the emitting particles (electrons) in hot spots and lobes of different FR-II sources, which is in apparent conflict with our result. Taking into account that the jet power cannot be significantly smaller than $P_{jet} \simeq 10^{47}\,\mathrm{erg\,s^{-1}}$, and that the kinematic estimate of the jet age should be correct to an order of magnitude, we can see that both approaches can only be reconciled if the parameter $\kappa \ll 1$ and/or the total lobe pressure is significantly larger than that of the magnetic field (i.e. if the lobes are dominated by the thermal population). Perucho et al. (2017) indicate that it is very unlikely that $\kappa \ll 1$, even for non-relativistic jets; the lobes could conceivably be dominated by the thermal population, however. Higher-quality d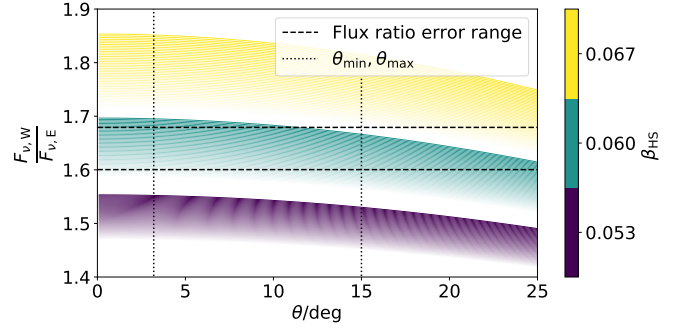ata will be needed to properly verify this hypothesis.